# Imaging Scheme for 3-D High-Frame-Rate Intracardiac Echography

## A Simulation Study

Soozande, Mehdi; Ossenkoppele, Boudewine W.; Hopf, Yannick; Pertijs, Michiel A.P.; Verweij, Martin D.; De Jong, Nico; Vos, Hendrik J.; Bosch, Johan G.

**DOI**
10.1109/TUFFC.2022.3186487

**Publication date**
2022

**Document Version**
Final published version

**Published in**
IEEE Transactions on Ultrasonics, Ferroelectrics, and Frequency Control

# Imaging Scheme for 3-D High-Frame-Rate Intracardiac Echography: A Simulation Study

Mehdi Soozande, *Student Member, IEEE*,
Boudewine W. Ossenkoppele, *Graduate Student Member, IEEE*,
Yannick Hopf, *Graduate Student Member, IEEE*, Michiel A. P. Pertijs, *Senior Member, IEEE*,
Martin D. Verweij, *Member, IEEE*, Nico de Jong, *Member, IEEE*,
Hendrik J. Vos, *Member, IEEE*, and Johan G. Bosch, *Member, IEEE*

***Abstract*— Atrial fibrillation (AF) is the most common cardiac arrhythmia and is normally treated by RF ablation. Intracardiac echography (ICE) is widely employed during RF ablation procedures to guide the electrophysiologist in navigating the ablation catheter, although only 2-D probes are currently clinically used. A 3-D ICE catheter would not only improve visualization of the atrium and ablation catheter, but it might also provide the 3-D mapping of the electromechanical wave (EW) propagation pattern, which represents the mechanical response of cardiac tissue to electrical activity. The detection of this EW needs 3-D high-frame-rate imaging, which is generally only realizable in tradeoff with channel count and image quality. In this simulation-based study, we propose a high volume rate imaging scheme for a 3-D ICE probe design that employs 1-D micro-beamforming in the elevation direction. Such a probe can achieve a high frame rate while reducing the channel count sufficiently for realization in a 10-Fr catheter. To suppress the grating-lobe (GL) artifacts associated with micro-beamforming in the elevation direction, a limited number of fan-shaped beams with a wide azimuthal and narrow elevational opening angle are sequentially steered to insonify slices of the region of interest. An angular weighted averaging of reconstructed subvolumes further reduces the GL artifacts. We optimize the transmit beam divergence and central frequency based on the required image quality for EW imaging (EWI). Numerical simulation results show that a set of seven fan-shaped transmission beams can provide a frame rate of 1000 Hz and a sufficient spatial resolution to visualize the EW propagation on a large 3-D surface.**

***Index Terms*— 3-D intracardiac echography (ICE), data rate reduction, electromechanical wave imaging (EWI), high-frame-rate ultrasound imaging.**

Manuscript received 24 February 2022; accepted 20 June 2022. Date of publication 27 June 2022; date of current version 27 September 2022. This publication is part of the project 3D-ICE (project number STW 14279) which is financed by the Dutch Research Council (NWO). *(Corresponding author: Johan G. Bosch.)*

Mehdi Soozande, Hendrik J. Vos, and Johan G. Bosch are with the Department of Cardiology, Erasmus Medical Center, 3015 GD Rotterdam, The Netherlands (e-mail: j.bosch@erasmusmc.nl).

Boudewine W. Ossenkoppele, Martin D. Verweij, and Nico de Jong are with the Department of Imaging Physics, Delft University of Technology, 2628 CD Delft, The Netherlands.

Yannick Hopf and Michiel A. P. Pertijs are with the Electronic Instrumentation Laboratory, Delft University of Technology, 2628 CD Delft, The Netherlands.

Digital Object Identifier 10.1109/TUFFC.2022.3186487

## I. Introduction

### A. Clinical Background

THE heart pumps blood with a rhythm determined by a group of pacemaking cells in the sinoatrial node. These cells generate an action potential that depolarizes cardiomyocytes. This action potential triggers the adjacent cells and propagates along the cardiac wall to generate global contraction. The conduction properties of cardiomyocytes and electrical pathways can be changed by normal aging or certain diseases, which leads to various types of arrhythmias. Atrial fibrillation (AF) is the most common cardiac arrhythmia and is the major cardiac precursor of stroke [1]. AF can be treated by RF ablation. A high-resolution 3-D anatomical mapping of electrical activity is required for localizing sources generating AF to plan the ablation procedure [2], [3]. A key feature of AF is its irregularity in time and space. Because the patterns of atrial activation change on a beat-to-beat basis, a series of consecutive activation maps is needed to cover the spatiotemporal variation in activation [4]. Intracardiac electroanatomical mapping is widely exploited to generate a 3-D surface map of atrial electrical activity [5].

### B. EW Imaging

Electrical excitation of cardiomyocytes is followed by a transient contraction after about 20–40 ms [6]. The electrical excitation is passed to neighboring cells and propagates along the atrial wall as a reaction–diffusion wave with a velocity of 0.5–2 m/s [7]. A high correlation between electrical and resulting mechanical activations has been reported in several studies [8]–[11] and this activation propagates as a wave-like phenomenon over the atrial wall: the electromechanical wave (EW). EW imaging (EWI) was introduced and has been developed by the group of Konofagou [7], [12]–[19] as a noninvasive ultrasound-based imaging method to map the electromechanical activations in the heart. Recent studies demonstrated a high correlation between the cardiac electrical activity and its consequent EW for healthy and arrhythmic cases in a simulation study [16], in the left ventricular wall [17], [18], atrial wall [15], and also in the walls of all four chambers [20].

EWI is accomplished in a two-stage process on ultrasound data [12]–[15]. In the first stage, tissue strain is estimated, commonly by a cross-correlation technique, along the axial direction on consecutive RF signals that are acquired at a motion-estimation rate (500–2000 Hz) [19]. In the second stage, EW onset is estimated by measuring the time at which the axial incremental strain departs from or crosses zero at a given pixel. We intend to image the propagation of the EW wavefront with a spatiotemporal resolution suitable for the identification of local electrophysiological phenomena. Since the EW velocities are in the order of 0.5–2 m/s and the desired spatial resolution is in the order of millimeters, we aim at a volume rate of 1000 Hz and a lateral resolution of 2–5 mm.

Current EWI can provide single-beat 2-D maps of the electromechanical wavefront (i.e., a cross-sectional image with activation times) with a lateral resolution of $<5$ mm. Since the EWs propagate throughout the entire heart, volumetric imaging is desirable to fully visualize their patterns. In previous studies, several 2-D images were acquired and processed separately. Then, a pseudo-3-D map was generated by combining these 2-D maps through ECG gating [20] and spatial interpolation. Recently, Grondin *et al.* [21] used a transthoracic matrix transducer to achieve 3-D EWI of the entire heart from the apical view. The narrow intercostal space and channel count limitations restricted their transducer size to 9.6 mm $\times$ 9.6 mm. In consequence, the lateral resolution was limited, to 5.8 at 40 mm. For the atria that are located much deeper ($>10$ cm), the lateral resolution will be lower. It would be interesting to see whether a higher resolution can improve strain mapping and reduce local inaccuracies in the EW patterns, especially in the atria.

### C. High-Frame-Rate 3-D ICE

Using an intracardiac echography (ICE) transducer can drastically reduce the required imaging depth for atrial EWI compared to the transthoracic apical view. Moreover, the possibility of using a higher central frequency compared to transthoracic transducers allows a higher spatial resolution in the atrial regions. Nowadays, ICE is widely exploited for RF ablation procedures to guide the electrophysiologists in septal puncture and to navigate the ablation catheter. However, this is limited to low-frame-rate 2-D-ICE. Several 3-D-ICE designs have been proposed [22]–[24], but these are not capable of imaging at high frame rates. A high-frame-rate 3-D ICE probe, in addition to delivering at least the functionality of conventional 2-D ICE, could provide a single-beat 3-D EW map. However, high-frame-rate 3-D ultrasound imaging introduces several challenges, including handling a high data rate generated by a large number of elements. Moreover, high volume rate allows just a few transmissions to illuminate the total volume, so a diverging wave transmission scheme is required. Possibilities for compounding are limited, and thus, SNR will be relatively low [25]. Furthermore, an intracardiac catheter imposes additional constraints on the transducer size, cable count, and power dissipation. Therefore, data reduction and an educated choice of design tradeoffs are crucial for high-frame-rate 3-D ICE.

### D. Data Rate Reduction by Micro-Beamforming

Micro-beamforming is a well-established method to reduce the channel count while preserving the image quality and SNR for volumetric imaging [26], [27]. In this method, element signals in a subaperture are mutually delayed and summed to form a single micro-beamformed signal from a predefined—steered—direction. The entire region of interest can thus be imaged by steering the subapertures to a sequence of different directions in, potentially, both azimuth and elevation, and implementing a parallel beamforming technique at the back-end system [28]–[30]. Since the final beamforming is based on the received data from subapertures with a relatively large effective pitch, grating lobes (GLs) can occur. Using relatively narrow transmit beams that are steered to the presteering directions can reduce the GL artifacts. Hence, a significant number of such narrow beams should be utilized to preserve the image quality [26]. Thus, increasing the number of elements per subaperture reduces the channel count but also reduces the achievable volume rate or field of view.

Wildes *et al.* [22] developed a 2-D transducer consisting of 60 $\times$ 14 elements with application-specific integrated electronics for volumetric ICE based on a 10-Fr (3.3 mm) catheter. A 2-D micro-beamforming approach was used to reduce the total receive channel count to 48 (along with power, transmit, and auxiliary signals leading to a total of 88 connections). Their method provided an imaging sector of 90° $\times$ 60° $\times$ 8 cm with a spatial resolution of 1.7 mm $\times$ 4.9 mm (azimuth $\times$ elevation) at a depth of 50 mm. They concluded that the achieved spatial resolution was sufficient for atrial imaging. To suppress the GLs formed by micro-beamforming, narrow beams were used in transmission, which limited the frame rate to 30 vol/s [22].

Implementing a 1-D (i.e., a 1 $\times$ $N$ subaperture) rather than a 2-D micro-beamformer introduces the GLs only in the direction in which the micro-beamforming is implemented. Therefore, the transmit beams need to be narrow only in the corresponding direction. Consequently, a 1-D micro-beamforming could provide a relatively high volume rate 3-D imaging by employing a set of fan-shaped diverging transmit beams that are narrow in the micro-beamforming direction and wide in the perpendicular direction (see Fig. 1). These asymmetric fan-shaped beams can cover a large volume of interest with a limited number of transmissions. These fan-shaped beams can be generated by a dual virtual source similar to the method proposed by Chen *et al.* [31] or a single virtual source behind a rectangular transducer, as shown in Fig. 1(b). Since a dual virtual source approach generates a curved transmit fan beam, it is less appropriate to be combined with a micro-beamforming approach. Therefore, we use a single virtual source approach in this study.

The size of the 1-D micro-beamformer should be chosen such that the needed reduction in channel count is achieved, while GL levels are kept sufficiently low. In the design of

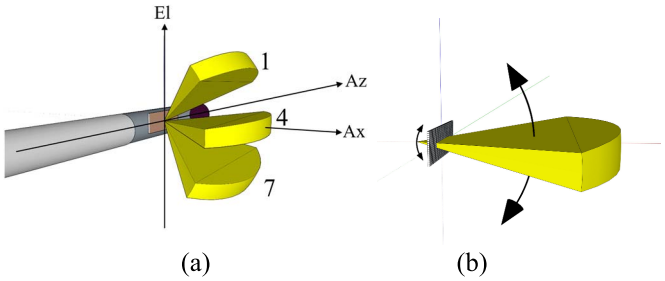


Fig. 1. (a) Schematic representation of the proposed side-looking transducer mounted in an intracardiac catheter. Azimuth (Az), elevation (El), and axial (Ax) directions are indicated on the corresponding axes. A set of three out of seven fan-shaped beams steered to different directions in elevation is shown to illustrate the transmit scheme. (b) Fan-shaped transmit beam is generated from a virtual source behind the transducer.

the high-frame-rate 3-D ICE many tradeoffs need to be made to realize an imaging scheme that satisfies the requirements for EWI while remaining within the constraints on transducer size and cable count, resulting from the small catheter size. Furthermore, the elements will be mounted on a pitch-matched application-specific integrated circuit (ASIC) containing all the required electronics, including high-voltage pulsers, low-noise amplifiers, time-gain compensation circuits, ADCs, and micro-beamformers, which are necessary to realize the proposed method [27], [32], [33]. The minimum pitch of the transducer elements is limited to 160 $\mu$m $\times$ 160 $\mu$m by the area required for the designed electronics.

In this study, we did not consider electronic noise and ultrasonic attenuation in the simulations since we are assuming that they are not limiting factors on the clutter and PSF image quality parameters we are studying here. They have been considered in the electronics design procedure [33] to achieve the desired imaging depth. Although these electronics design choices put some limits on the transducer layout and the imaging scheme as mentioned in Sections I and II, fully describing these choices is out of the scope of this article.

### E. 3-D ICE Imaging Scheme Design

In this study, we develop a novel imaging scheme for high-frame-rate 3-D ultrasound imaging with a matrix intracardiac catheter as sketched in Section I-D and optimize the transducer design and imaging scheme for intracardiac EWI. The main goal is to enable volumetric imaging with a sufficient frame rate and image quality for EWI while reducing the data rate to realistic values. The proposed method consists of implementing a 1-D micro-beamforming in the elevation direction to reduce the data rate. By combining this with the transmission of fan-shaped beams, a high-frame-rate is enabled, while GLs in the elevation direction are suppressed. The proposed method achieves further reduction of the GL artifacts and improved contrast to noise ratio (CNR) by implementing angular-weighted coherent compounding. We will discuss the optimization of the imaging scheme (transmit frequency, microbeamformer size, and transmit beam divergence) to achieve the desired channel count reduction while providing a sufficient frame rate and image quality for EWI. Finally, we evaluate the proposed imaging scheme in a series of simulations. The novelty of this work lies in an imaging scheme optimized for dedicated integrated circuitry to realize high-frame-rate 3-D ICE suitable for EWI.

## II. Materials and Methods

### A. Imaging Scheme Design: Parameters

We strive for a 3-D ICE design with a frame rate of 1000 Hz, an imaging depth of 10 cm, an opening angle of 70° $\times$ 70°, and a lateral resolution of 5 mm to be able to realize the 3-D EWI of the left atrium from the right atrium.

For a depth of 10 cm, the pulse repetition frequency (PRF) is limited to 7.7 kHz by the round-trip travel time of the ultrasound waves assuming a speed of sound of 1540 m/s. Therefore, a maximum number of seven transmissions are available to acquire the entire region of interest, and we will always use this number of transmissions in our scheme.

We base the design of the matrix transducer on a 10-Fr intracardiac catheter, which limits the transducer size to 3 mm in the elevation direction [see Fig. 1(a)] and the number of cables to a maximum of 100 [22], [34]. The aperture of the matrix array is rectangular, with the shortest axis perpendicular to the ICE probe shaft. We consider square elements with a pitch of 160 $\mu$m, imposed by the area needed for the pitch-matched application-specific electronics [32]. Choosing such a large pitch (50%–80% of the wavelength for the assumed frequency range of 5–8 MHz) introduces GLs in image reconstruction and also secondary waves in diverging wave transmission. To counteract these, we optimize the central frequency in the given range to suppress the secondary waves. In addition, an angular weighting function is applied to a conventional delay and sum to reduce the GLs. Based on the chosen pitch and catheter size constraints, we consider a matrix array of 18 $\times$ 64 elements.

The imaging scheme consisting of steered fan-shaped diverging transmit beams will be used with 1-D micro-beamforming in the elevation direction and acquisition of all element-level signals in the azimuthal direction. Furthermore, angular weighted coherent compounding will be used to reduce GL levels. Transducer size, pitch, number of transmissions, and imaging depth are fixed in this study, whereas the other features are optimized in a simulation study.

### B. Steerable Fan-Shaped Transmit Beam

A single virtual source was used to generate the desired fan-shaped beam. In this approach, the beam divergence in azimuth and elevation is not independent. First, we determined the virtual source location based on the transducer size and desired beam divergence in the elevational direction, and then, the effective transducer size in azimuth was determined to achieve the required beam divergence in that direction (see Appendix I).

### C. Angular Weighted Averaging

A voxel-based delay and sum is proposed to reconstruct an intermediate full volumetric image corresponding to each transmission. Since only a narrow region is insonified in the elevation direction for each transmission, reconstructing

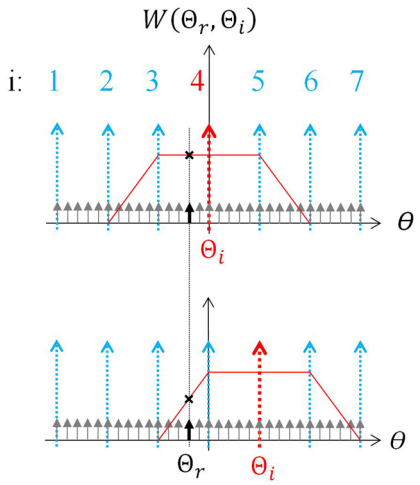


Fig. 2. Applied weights $W(\Theta_r, \Theta_i)$ as a function of the reconstruction elevation direction $\Theta_r$ for different transmit beams. Blue arrows show all transmission directions and red arrow shows the current transmission direction with its corresponding angular weighting function. Black arrows show the reconstruction directions and the bold black arrow shows an example of receive line with its corresponding weights (black cross) when the transmit direction is $\Theta_i$.

regions far from this transmission direction only adds noise to intermediate images. In addition, the receive beam profile contains strong GLs at directions corresponding to the large effective pitch associated with the micro-beamformer size [26]. Hence, the final volumetric image is obtained by applying angular weighting functions to the intermediate images in order to suppress the noise and GLs in noninsonified regions and also improve the image quality by coherent compounding of overlapping regions using

$$I(R, \Theta_r, \varphi) = \sum_{i=1}^{7} W(\Theta_r, \ \Theta_i) \sum_{m=1}^{N_{\mu BF}} \sum_{n=1}^{N_{Az}} S_{m,n}\left(t - \sigma_i - \sigma_{m,n}\right) \tag{1}$$

where $I(R, \Theta_r, \varphi)$ is the reconstructed RF sample in a spherical coordinate system, $W(\Theta_r, \Theta_i)$ is the weighting function (as shown in Fig. 2) corresponding to the transmit direction $\Theta_i$, $S_{m,n}$ is the micro-beamformed signal of a subgroup at the elevation position $m$ and azimuthal position $n$ in the transducer array, $\sigma_i(R, \Theta_r, \varphi)$ is the transmit delay, $\sigma_{m,n}(R, \Theta_r, \varphi)$ is the receive delay, and $\Theta_i$ is the transmit/presteering direction.

Fig. 2 shows the angular weights as a function of the reconstruction line direction for different transmission directions. To avoid abrupt changes in image intensity, the angular weights have some overlap with their neighboring transmissions [33].

## D. Simulation Setup

The simulation study consists of three steps. First, the azimuthal beam divergence and central frequency in a range of 20°–45° and 5–8 MHz, respectively, are mutually optimized to provide an acceptable tradeoff among the imaging opening angle, transmit beam quality, and spatial resolution. Transmit beam quality in diverging wave imaging is known to be susceptible to the occurrence of so-called axial lobes or secondary pulses [37], [38], related to imperfect signal cancellation of late-arriving element signals from arrays with pitch larger than half a wavelength. Since the quality of the transmitted wave is very important for our image quality, we will first investigate and optimize the temporal profile of the transmitted diverging wave in our simulations.

Second, transmit beam divergence in elevation will be determined based on GL artifacts and the intensity uniformity between transmissions. Finally, the image quality will be evaluated for a micro-beamformer size ranging between 1 (no micro-beamforming) and 4 to achieve an acceptable tradeoff between the desired image quality and data rate reduction. The imaging parameters are summarized in Table I. All simulations are performed in Field II [35].

TABLE I
IMAGING PARAMETERS

| Parameters | Value |
|---|---|
| Transducer size | 2.88 mm×10.24 mm |
| Pitch | 160 μm ×160 μm |
| Kerf | 20 μm |
| Number of elements | 18×64 |
| Micro-beamformer size | 1-4 elements* |
| Imaging depth | 10 cm |
| Frame rate | > 1000 Hz |
| Transmit beam | Steerable Fan beam |
| Number of transmissions | 7 |
| Transmission beam (azimuth) | Direction: 0°; divergence: 20°-45°* |
| Transmission beam (elevation) | Direction: -30° to 30°; step:10°; divergence: 10.7°, 12.5°-20°*; step: 2.5° |
| Central frequency | 5-8 MHz* |
| Sampling frequency | 4×central frequency |
| Transmit apodization | 2-D Tukey window with cosine fraction 0.2 |

* These parameters are evaluated within the given ranges to optimize the imaging scheme.

## E. Numerical Phantoms

*1) Static Phantom:* A 3-D numerical phantom, a cube with an edge length of 100 mm containing hyperechoic and hypoechoic spherical regions with diameters of 2, 4, 6, and 10 mm, highly reflective points and background point scatterers with an average density of $0.2/\lambda$, has been used in Field II simulations. The relatively low point scatterer density is chosen to limit simulation time for this large-size cubic phantom and the high number of transducer elements. In addition, a single-point scatterer at a depth of 50 mm is simulated to determine the point spread function (PSF).

*2) Beating Left Atrium:* To evaluate the proposed high-frame-rate imaging scheme in a dynamic environment, a spherical

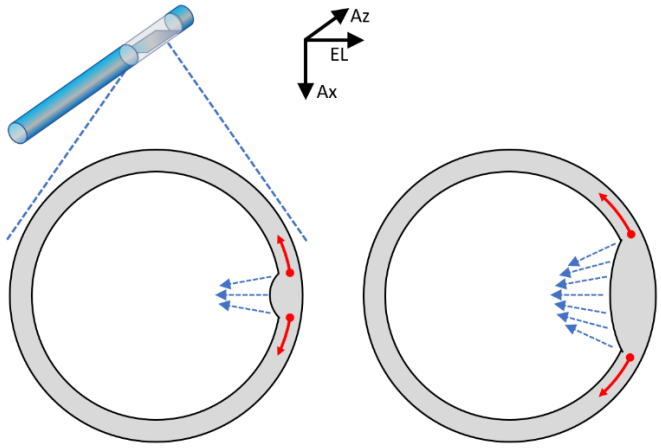


Fig. 3. Schematic cross sections of the 3-D left atrium numerical phantom (radius 50 mm and thickness 3 mm). Left: wave is introduced as a radial wall thickening (blue arrows). Red arrows show the circumferential electromechanical wavefront propagation direction. Right: wavefront propagation after ∼10 ms (thickness/excursions not to scale).

shell with an outer diameter of 50 mm and a thickness of 3 mm has been simulated mimicking a left atrium. The center of the sphere is at an axial distance of 50 mm, equivalent to imaging the left atrium from the center of right atrium. A circumferentially propagating wave has been introduced to this phantom by applying a radial thickening with an amplitude of 10 mm/s (10 $\mu$m/frame). The atrial thickening initiates from a single point and propagates omnidirectionally along the atrial wall with a velocity of 2 m/s [7]. A cross section of the beating left atrium numerical phantom is shown in Fig. 3.

We use 1-D axial cross correlation (two cycles Tx pulse, 20-sample I/Q) to estimate the frame-to-frame tissue displacement. Since simulating a 3-D numerical phantom with a matrix array in Field II is very time consuming, we limit our simulations to only three pairs of consecutive volumetric datasets acquired at an interval of 1 ms within each pair (i.e., mimicking a frame rate of 1000 Hz). The consecutive pairs of datasets have been simulated for three time points, $t = 0$, 10, and 20 ms to show the concept of EWI. The final map of tissue displacement (actually displacement over 1 ms in the direction of the ultrasound beam, so the axial tissue velocity component) has been generated by applying an image intensity-based mask to the displacement data to only visualize the atrial wall. In addition, another mask based on tissue displacement has been applied to the displacement map to exclude nonmoving tissue.

### F. Evaluation Criteria

The performance of various combinations of transmission and micro-beamforming schemes has been evaluated, as assessed by the widths of PSF at −6 dB (azimuthal and elevational resolutions), the sidelobe level, the GL level, and the CNR. The sidelobe level is defined as the peak level of the highest sidelobe compared to the main lobe in dB, and the GL level is defined as the peak level at the theoretically expected GL direction. These two were measured by imaging only one scatterer in the field of view. The CNR is calculated using [36]

$$CNR = \frac{\mu_s - \mu_c}{\sqrt{(\sigma_s^2 + \sigma_c^2)/2}} \tag{2}$$

where $\mu_s$ and $\mu_c$ are the mean amplitudes and $\sigma_s$ and $\sigma_c$ are the standard deviation of the gray levels in the speckle and anechoic cyst regions, respectively, of the 3-D numerical phantom.

Imaging with a limited number of diverging beams and micro-beamforming may result in angle-dependent changes in image characteristics. To evaluate these effects, a lateral shift-variance plot (LSV-plot) [37] is used. An LSV-plot is constructed for a given imaging system by imaging a point scatterer shifting laterally. For each lateral position, a PSF is calculated and stacked to the other PSFs to form a 2-D image. The entire image is normalized to its maximum value and plotted in a decibel scale. If there is little position dependence, the plot will be invariant along the diagonal; otherwise, deviating structures will be visible revealing the nature of the position dependence. In this study, a point scatterer at a distance of 50 mm from the center of the transducer is shifted along the elevation direction from −45° to 45° with a step of 1° to create the LSV-plot.

## III. Results

### A. Imaging Scheme Optimization

*1) Transmit Central Frequency and Azimuthal Divergence Angle:* When evaluating the transmitted diverging waves, we found significant secondary pulse levels in the transmitted time signals. In Fig. 4(a) where the envelope of the transmit pulse is shown for all azimuth angles, it can be seen that the secondary pulse is present over a large range of the opening angle and gets longer for larger angles, following the primary short pulse after a few microseconds. Fig. 4(b) shows the transmit pulse generated by a transducer with a 45° divergence and 7.5-MHz center frequency in a point 50 mm from the transducer, at an angle of 40°.

We evaluated how the pulse shape depended on the beam divergence and transmit central frequency. The level of the secondary pulse has been measured at points located on a spherical surface with a radius of 50 mm ranging from −45° to 45° in both azimuth and elevation directions. The maximum of the secondary pulses measured in different directions is shown in Fig. 5(a) as a function of central frequency and beam divergence. The function has a triangular local minimum region in the frequency band of 5.3–7.5 MHz and the azimuthal beam divergence of 25°–45°. Any local minimum close to the triangle hypotenuse will achieve low secondary pressure levels for a relatively high central frequency and opening angle. To show the effect of these secondary pulses, images of point scatterers made with transmit beams with different secondary pressure levels are reconstructed. Fig. 5(b) shows that the larger secondary pulse [corresponding to the black dot in Fig. 5(a)] will interact with the scatterers to show prominent secondary echoes of scatterers (arrows), whereas in Fig. 5(c), where the transmit beam has a lower secondary-pulse pressure level [corresponding to the white dot in Fig. 5(a)], the

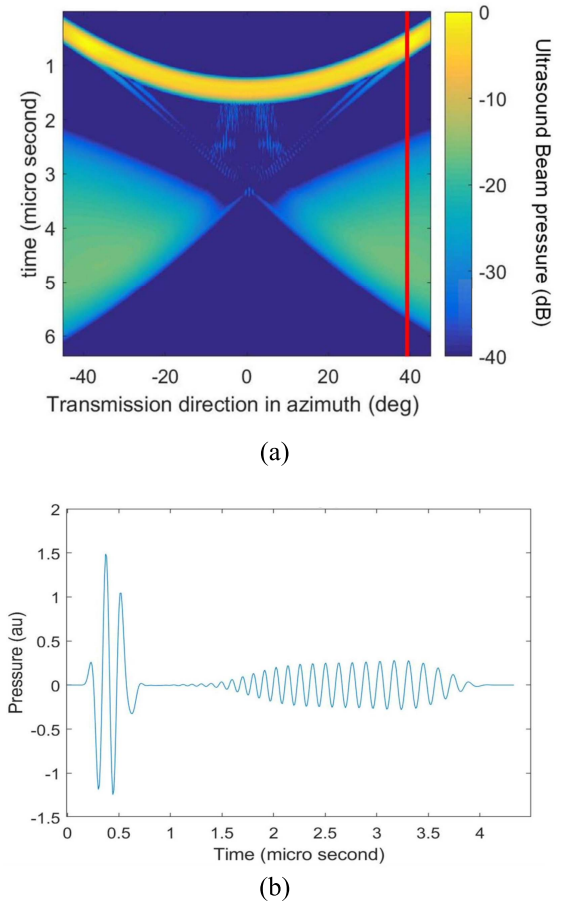


Fig. 4. Transmitted pressure profile of a diverging wave as a function of time and azimuth angle at typical imaging depth of 50 mm, $f = 7.5$ MHz, and divergence $= 45°$. (a) Envelope of the pressure from $-45°$ to $45°$ (red line indicates the position of the point used to acquire the 1-D signal in (b). (b) Time-domain pressure signal at 40° azimuth. The secondary pulse is observed as a longer pulse with lower amplitude compared to the main pulse.

secondary echoes are almost invisible. We choose a central frequency of 6 MHz and an azimuthal beam divergence of 35° and these values will be used as bases for the rest of simulations.

*2) Elevational Beam Divergence and Intensity Ripple:* With the proposed transducer size and the chosen azimuthal beam divergence of 35°, the single virtual source technique can provide an elevational beam of 10.7°. The transmit beam profile for this elevational beam divergence is shown in Fig. 6, which shows an intensity ripple over elevational angle of −3.6 dB. To reduce this ripple, we would need to increase elevational beam divergence. To achieve the wider elevational beam divergences of 12.5°, 15°, 17.5°, and 20°, the effective number of elements in azimuth was reduced from 64 to 56, 47, 41, and 36 elements, respectively. This azimuthal apodization was needed to maintain the 70° azimuth opening angle when bringing the virtual focus closer to the probe for more elevational divergence. The intensity ripples between two adjacent transmissions are listed in Table II for different elevational beam divergences as a measure of nonuniformity. The results show a lower intensity ripple for broader beam, which indicates more uniform image intensity along the elevation direction.

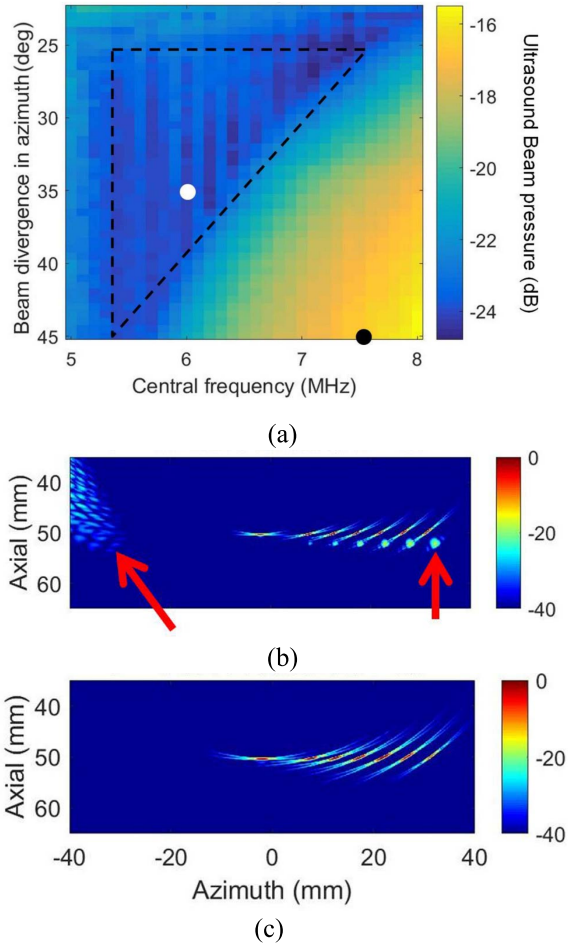


Fig. 5. (a) Maximum of secondary pressure peaks as a function of central frequency and azimuthal beam divergence. Reconstructed images based on a fully sampled array for a central frequency and azimuthal beam divergence of (b). $f = 7.5$ MHz and $\varphi_{az} = 45°$ [black point in (a)] and (c). $f = 6$ MHz and $\varphi_{az} = 35°$ [white point in (a)]. Red arrows show the secondary reflection and GL caused by poor destructive interference of waves transmitted from each individual element.

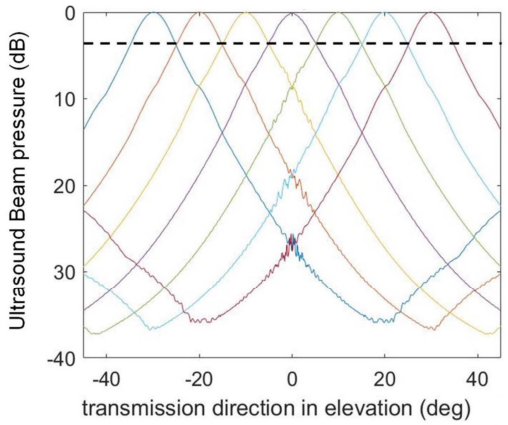


Fig. 6. Transmit beam profile in the elevation direction for an elevational beam divergence of 10.7°. The horizontal dashed line shows an intensity ripple level of −3.6 dB.

*3) Elevational Beam Divergence and GLs:* In the next step, the effect of elevational beam divergence on the GL level has been evaluated. The GL directions for a micro-beamformer size of 2, 3, and 4 are 53°, 32°, and 24°, respectively, at the

TABLE II
TRANSMIT BEAM PROFILE NONUNIFORMITY MEASURED BY THE INTENSITY RIPPLE BETWEEN TWO CONSECUTIVE TRANSMISSIONS

| Elevational beam divergence | Intensity ripple (dB) |
|---|---|
| 10.7° (possible minimum) | -3.6 |
| 12.5° | -3.3 |
| 15° | -2.4 |
| 17.5° | -1 |
| 20° | -0.4 |

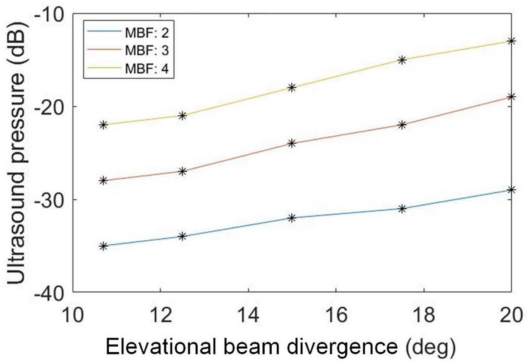


Fig. 7. Transmit pressure at GL directions, normalized to transmit pressure at main lobe for different beam divergences.

chosen frequency of 6 MHz. The acoustic pressure at GL directions has been compared for elevational beam divergence of 10.7°, 12.5°, 15°, 17.5°, and 20°. Fig. 7 shows that increasing the transmission elevational beam divergence intensifies the GL levels. An elevational beam divergence of 10.7°, which is the narrowest possible divergence, with a beam separation of 10°, provides the lowest GL level and highest SNR at the cost of some nonuniformity in image intensity. We chose the elevational beam divergence of 10.7° and used this value in the remainder of the simulations. With this elevational divergence, the set of steerable fan-shaped beams provides an imaging field of view of 70° (width of insonified region at −3 dB) in the elevation direction.

### B. Imaging Performance Evaluation

The angular weighted coherent compounding approach is evaluated for a micro-beamformer of 2–4 elements by reconstructing images of a single-point scatterer. Applying the proposed angular weighting function reduces the GL level to a value that we will refer to as the GL residual (GLR). Fig. 8(a) shows the effect of using angular-weighted coherent compounding compared to uniform coherent compounding for a micro-beamformer size of three elements. This angular weighted coherent compounding reduces the GL levels by 28, 16, and 13 dB for micro-beamformer sizes of 2, 3, and 4, respectively. Elevational PSFs for angular-weighted compounding for different micro-beamformer sizes are shown in Fig. 8(b). The width of PSF at −6 dB is shown in Fig. 9 for different imaging depths in both azimuthal and elevational directions.

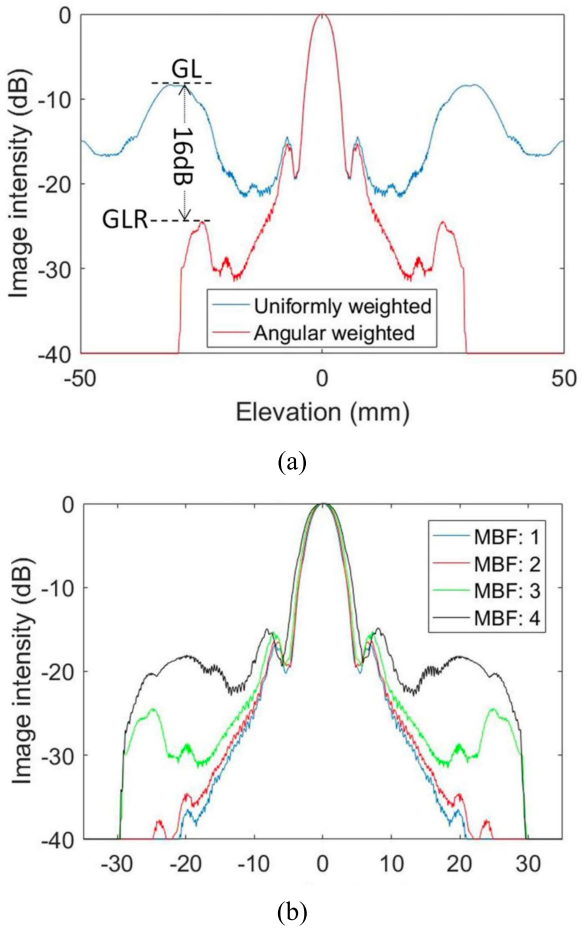


Fig. 8. (a) PSF in the elevational direction, for a single-point scatterer at 50 mm depth which is reconstructed by uniform coherent compounding and reconstructed by angular-weighted coherent compounding. GL level and GL residual level are shown for uniform coherent compounding and angular-weighted compounding, respectively. (b) PSF for angular-weighted compounding for different micro-beamformer sizes and elevational beam divergence of 10.7°.

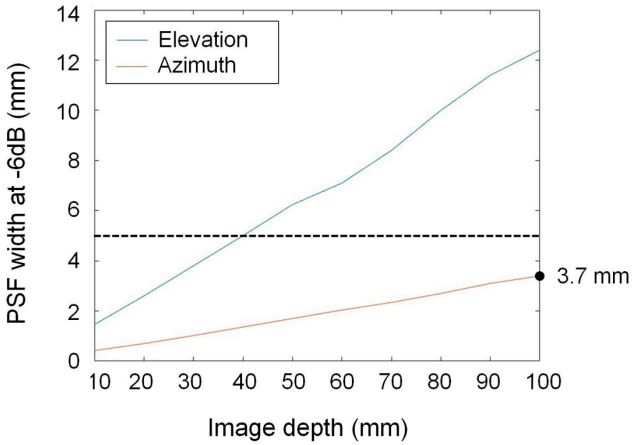


Fig. 9. Lateral resolution as a function of depth in azimuth and elevation directions for a micro-beamformer size of three elements. The horizontal dashed line indicates the desired lateral resolution for EWI.

The spatial variance of the proposed imaging scheme in the elevation direction is evaluated by an LSV-plot. Fig. 10(a) shows the LSV-plot for micro-beamforming size 3. Although the effect of the seven transmit beams is visible as nonuniform

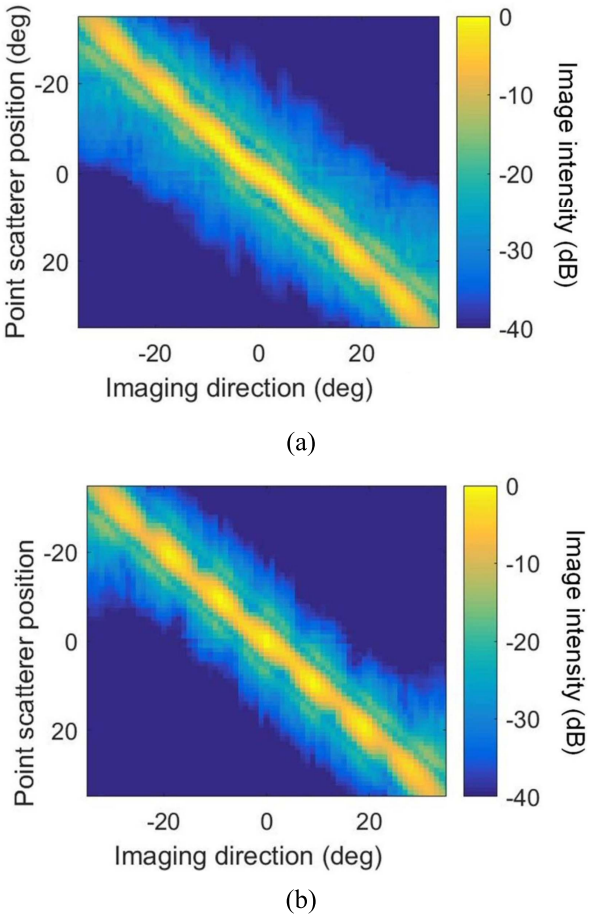


Fig. 10. LSV-plot of a single-point scatterer at different positions ranging from −35° to 35° in the elevation direction, which is reconstructed by (a) proposed weighting function and (b) triangular weighting function.

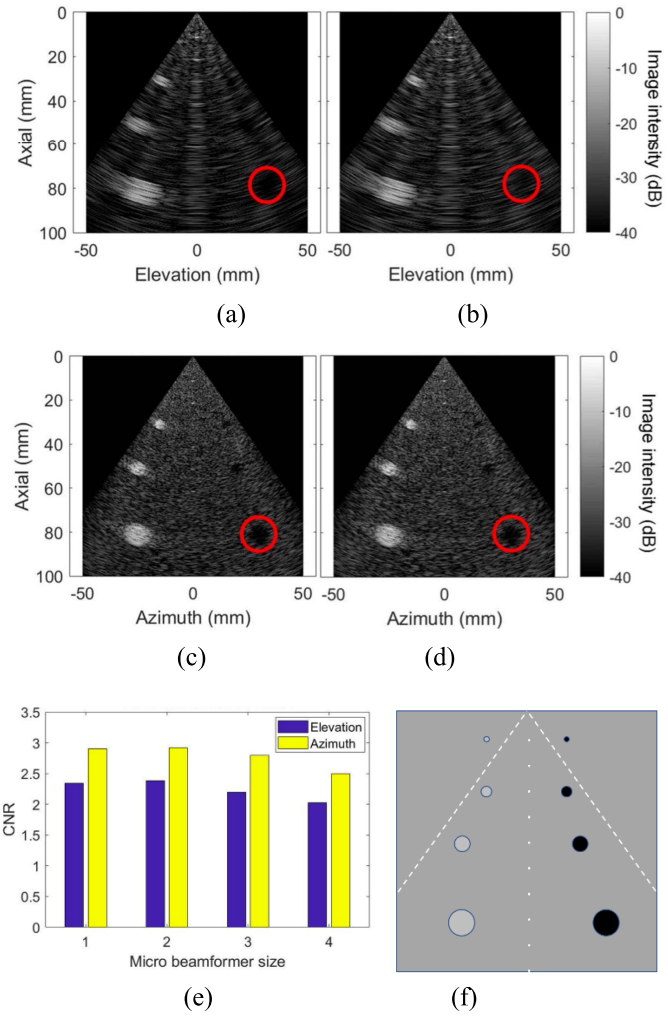


Fig. 11. Reconstructed images of a tissue-mimicking phantom in (a) elevation direction for a fully sampled array, (b) elevation direction for a micro-beamformer size of three elements, (c) azimuth direction for a fully sampled array, and (d) azimuth direction for a micro-beamformer size of three elements. Red circles show hypoechoic regions where the CNR was calculated. (e) CNR in azimuth and elevation for different micro-beamformer sizes. (f) Schematic representation of tissue-mimicking phantom, rotated to (a) and (b) elevation or (c) and (d) azimuth plane.

image intensity in this plot, the lateral resolution, sidelobe level, and GL levels are fairly diagonally uniform. In addition to lateral shift variability, the LSV-plot was used to compare the proposed angular weighting function with the conventional triangular weighting function [37]. Since the proposed method compounds a high number of transmissions to reconstruct a single receive line, the LSV-plot is more diagonally uniform and has a narrower main lobe. However, it produces higher clutter around the main lobe, as shown in Fig. 10.

The numerical tissue-mimicking phantom has been imaged to evaluate the image quality in terms of CNR for various micro-beamformer sizes. The clutter level is increased in hypoechoic regions by increasing the micro-beamformer size [see Fig. 11(a)–(d)], which reduces the CNR in both elevation and azimuth planes, as shown in Fig. 11(e). Narrow transmission beams with a large separation angle cause nonuniform image intensity along the elevation direction, as expected from Fig. 6. Fig. 11(a) and (b) shows that the axial resolution (estimated at 0.8 mm) is not affected by the microbeamforming, as expected, and seems sufficient with respect to the atrial wall thickness.

*1) High-Frame-Rate Imaging of a Beating Atrium Phantom:* A rendered volumetric image of the beating left atrial numerical phantom has been generated with a micro-beamformer size of three elements and is shown in Fig. 12. A quarter of the top hemisphere has been removed to show the wall thickness in azimuthal, elevational, and $c$-plane. We can clearly see the spherical object mimicking left atrium. The atrial wall appeared thicker in the elevational direction, which is caused by the lower elevational resolution. A combination of fan-shaped transmit beams and the proposed weighting function successfully suppressed the GLs and no obvious GL is visible. However, nonuniform image intensity is rather visible in the elevation direction.

Fig. 12(a)–(c) shows the tissue displacement maps on three orthogonal planes, namely, azimuthal, elevational, and $c$-plane, which were calculated at $t = 1$, 11, and 21 ms. The EW has initiated from a point shown by the blue arrow in Fig. 12(a) and propagated omnidirectionally on the atrial surface. Fig. 12(b) and (c) shows the propagation of the EW at 11 and 21 ms after the wave generation. The electromechanical wavefront is clearly visible and the color gradient indicates the

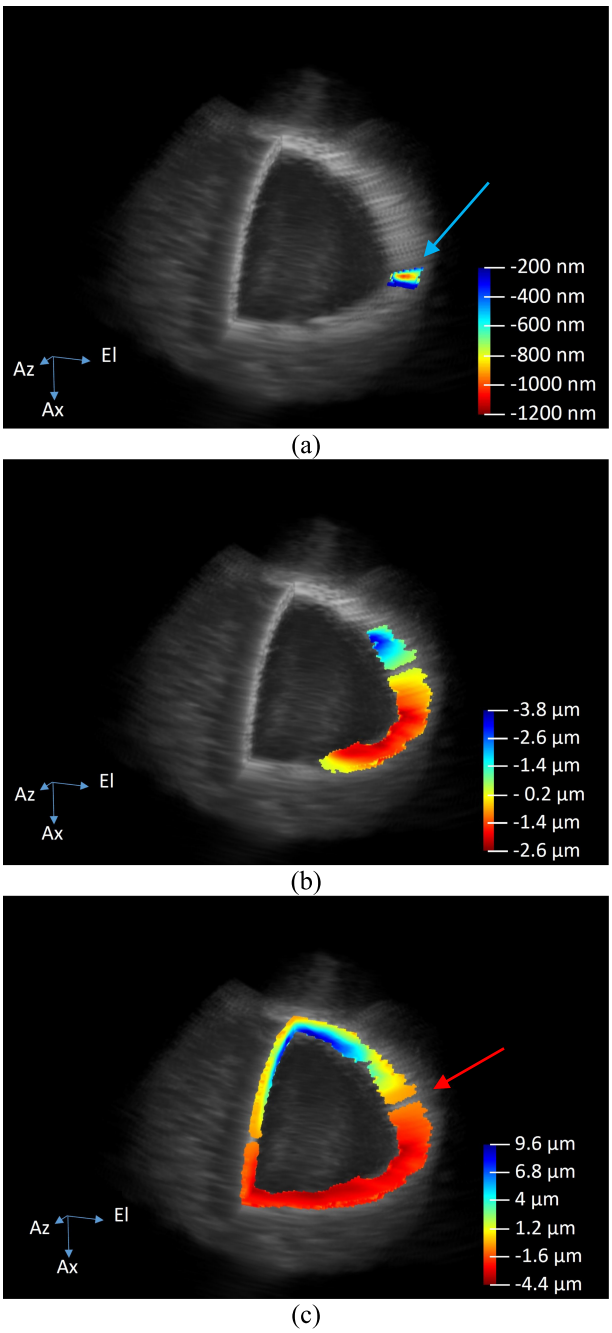


Fig. 12. Tissue frame-to-frame axial displacement map corresponding to EW propagation at (a) $t = 1$ ms, (b) $t = 11$ ms, and (c) $t = 21$ ms plotted on orthogonal planes. The blue arrow on (a) shows the initial point of EW and the red arrow on (c) shows the location at which the displacement is perpendicular to the ultrasound axial direction and cannot be estimated. The probe is located left side of the atrium at 50-mm distance. Please note that the color scale represents axial displacement over 1 ms, so a displacement of 10 $\mu$m is equivalent to an axial velocity component of 10 mm/s.

radial strains. The EW map was masked by an intensity-based mask derived from the $B$-mode images. There is no unwanted motion detection on other parts of the region of interest. The red arrow in Fig. 12(c) shows a region where the radial motion is purely perpendicular to the ultrasound wave axial direction. Therefore, the 1-D axial cross-correlation technique could not detect this displacement.

## IV. Discussion and Conclusion

In this study, we have proposed a novel imaging scheme for high-frame-rate 3-D ultrasound imaging with a matrix intracardiac catheter. The main goal is to enable volumetric imaging with a sufficient frame rate and image quality for EWI while reducing the data rate to realistic values. The proposed method consists of three main parts: 1) implementing 1-D micro-beamforming in the elevation direction to reduce the data rate; 2) transmitting fan-shaped beams to suppress GLs in the elevation direction while providing a high frame rate; and 3) angular-weighted coherent compounding to further reduce the GL artifacts and improve CNR.

The transducer consists of 64 $\times$ 18 elements with a pitch of 160 $\mu$m, which is larger than half of the wavelength at 5–8 MHz, giving rise to spatial aliasing. Generating a diverging wave from an array with such pitch can lead to a secondary, trailing, pulse as a result of poor destructive interference of the signals from the adjacent elements—see Fig. 4. This secondary pulse will also interact with scatterers, leading to secondary reflections in the reconstructed images and thus increased axial clutter levels [38], as shown in Fig. 5(b). Such axial lobes were previously reported by Rodriguez-Molares *et al.* [39] for coherent plane wave compounding. They theoretically analyzed the secondary-pulse formation and proved that late-arriving transmit waves lead to delayed echoes that render as axial lobes. They showed that in a densely sampled array (pitch $< \lambda/2$), late-arriving signals will cancel each other out, which reduces the axial lobe level. In this work, we reduce the secondary pulse level by carefully choosing the central frequency and azimuthal beam divergence for the given array configuration [see Fig. 5(a)].

We intend to image the EW wavefront propagation in 3-D with sufficient spatial resolution by employing a high volume rate of 1 kHz. This is sufficient for local motion estimation over the whole volume, but previous research on EWI [19] suggests that while a local motion detection rate of 0.5–2 kHz is required, a slower rate might be sufficient for the motion sampling (the generation of the strain maps), leaving room for more lenient interleaved spatial interrogation. Provost *et al.* [19] reported that a mapping rate of 120 Hz would suffice since the highest frequency content of the EW would be around 50 Hz. However, since we operate at higher spatial resolution and the EW is a complex reaction–diffusion wave, we are not sure that this bound is valid in our situation. Therefore, we preferred to pursue the full 1-kHz volume rate. Furthermore, this also opens the way to other high-frame-rate applications such as shear wave elastography and ultrafast Doppler.

A high ultrasound frequency was preferred to achieve a sufficient lateral resolution for EWI. On the other hand, a large opening angle was needed to capture the entire left atrium. As shown in Fig. 5, a central frequency of 6 MHz and an azimuth opening angle of 35° will result in a low secondary-pulse pressure level. Furthermore, at these values, small variations in the fabrication process and delay quantization frequency will not have large effects on the secondary pressure level.

The elevational beam divergence is subject to a tradeoff between the image intensity uniformity, SNR, and GL levels. A wider transmission reduces image intensity nonuniformity but also generates a higher acoustic pressure in the GL direction. Since we use a single virtual source method, the effective aperture size in the azimuthal direction must be reduced to generate divergences larger than the smallest realizable divergence of 10.7°. Consequently, wider elevational divergence reduces SNR.

To achieve a high SNR and low GL levels, we selected a divergence of 10.7° in the elevation direction. This leads to a nonuniform image intensity in the elevation direction. This nonuniformity is not expected to influence the performance of the proposed method for EWI since the tissue displacement is measured in the axial direction. Nonuniformity of the transmitted power in the $B$-mode can be compensated for by applying a weighting function to the reconstructed images. However, this corrects the nonuniform image intensity at the cost of producing a nonuniform SNR.

By using a dual virtual source technique similar to that proposed by Chen *et al.* [31], the dependence between the azimuthal and elevational beam divergence can be avoided such that all aperture sizes can be used. However, we found that using a dual source was an unsuitable solution for our design since beams appeared to curve in the elevation direction when steering to large angles, which decreases the overlap between the transmit beam directions and the micro-beamforming presteering direction.

The proposed set of steerable fan-shaped beams can insonify a region of 70° × 70°, which is sufficient to cover the entire left atrium from the center of the right atrium, as shown in Fig. 12.

Fig. 12 shows a rendered volumetric image of the left atrium. Since the lateral resolution is lower in elevation, the atrial wall seems to be thicker in this direction in comparison to the azimuthal direction. The image intensity nonuniformity caused by narrow transmit beams in elevation is visible as darker traces. In addition, there are some artifacts at lower depths that are caused by high clutter level of the proposed method, as shown in Fig. 10(a). The high clutter levels are mainly caused by implementing 1-D micro-beamforming in elevation, as shown in Fig. 8(b). This can reduce the tissue displacement estimation accuracy. Hence, more advanced beamforming techniques, such as minimum variance and clutter suppression techniques, might be further used to improve the motion estimation and EW tracking.

In this study, we have evaluated the imaging performance of the proposed method in a series of simulations in which we tried to mimic the *in vivo* situation. However, there are more practical challenges, which could not be investigated in these simulations. For instance, signal-to-noise ratio or detecting EWI onset in the presence of noise, motion, and anisotropic tissue scattering are important *in vivo* challenges, which should be evaluated extensively in *in vitro*, *ex vivo*, and/or *in vivo* studies.

The tissue motion has been estimated by 1-D cross correlation and shown in Fig. 12(a)–(c). The atrial wall thickening has been successfully shown as a radial gradient in the frame-to-frame displacement map. However, this is only a limited and highly simplified proof of principle of the EW onset detectability. The EW onset is usually tracked by finding a zero crossing on strain rate data. Since only three pairs of high-frame-rate volumes have been simulated in this study, a full map of EW is not generated. Nevertheless, the EW onset is clearly visible on the tissue displacement maps. The EW approximately propagated one eighth of the sphere circumference at 10 ms, which is equal to a velocity of 2 m/s. These intermediate results show the general imaging performance of the proposed method and its potential for EWI, although this remains to be confirmed by more realistic simulations and shown in experiments.

The proposed method provides an azimuthal lateral resolution smaller than 3.7 mm on the entire imaging depth (10 cm), which is likely sufficient for EWI [7]. The diameter of the targeted 10-Fr catheter limits the transducer size to 3 mm in the elevation direction, leading to a poorer lateral resolution in this direction. Therefore, at depths beyond 40 mm, the resolution in the elevation direction exceeds 5 mm. The results show that the proposed method outperforms the state of the art on 3-D ICE in terms of frame rate [22]. Moreover, previous works on pseudo-3-D EWI showed that 2–4 planes already provided additional information for EWI of the atrium [14], [20] to reconstruct a volume by spatial interpolation. Our proposed method provides a volume consisting of 12 planes in the elevation direction (natural divergence of transducer at 6 MHz is 6°), which can thus provide even more 3-D details. In addition, the proposed method acquires the 3-D EW at a single heartbeat, which is more suitable than ECG-gated 3-D EWI for mapping cardiac arrhythmia. With this increase in 3-D detail, the proposed design has the potential to improve the accuracy of electromechanical activation mapping and to detect smaller and nonperiodic arrhythmogenic sources.

In this study, we have focused on EWI for mapping AF. However, recent studies showed that EWI can be useful for mapping other cardiac conduction system abnormalities and arrhythmia such as atrial flutters [18] or accessory pathways in patients with the Wolf–Parkinson–White syndrome [13].

Many aspects are still unclear regarding EWI. The relation between electrical activation and mechanical contraction is determined by a combination of biochemical and mechanical interactions of partially unknown properties. Especially in cases of nonuniformities or pathology, this relation will be very complex. Whether the mechanical response alone can be used for patient-specific diagnosis remains to be shown. Nevertheless, measuring the mechanical response with high spatiotemporal resolution is important to gain insight here.

A practical probe implementation requires channel-count reduction since the number of elements far exceeds the number of cables that can be accommodated. A 1-D micro-beamforming scheme reduces the data rate by a factor equal to the number of elements per subaperture. We have shown that a data rate reduction by a factor of 2 results in negligible image quality loss. A micro-beamformer size of 3 or 4 introduces some imaging artifacts. The PSF analysis has shown that the elevational resolution changes negligibly by increasing the micro-beamformer size to 3 but increases from 6.1 to 7 mm

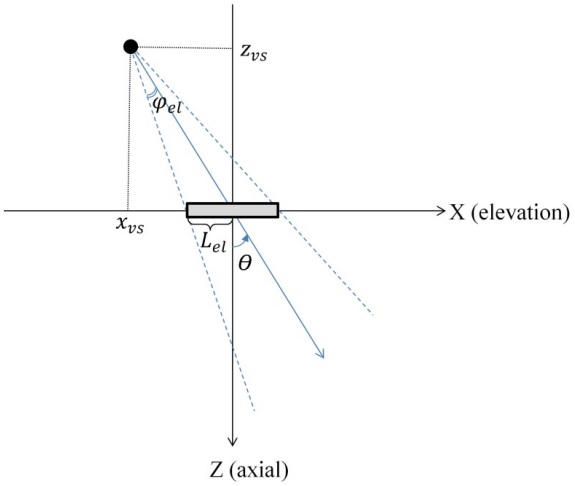


Fig. 13. Generating a fan-shaped transmitting beam with a divergence of $\varphi_{el}$ in elevation and steered to $\theta$ using a virtual source behind the transducer.

by utilizing a micro-beamformer of four elements at 50-mm imaging depth. Fig. 8(b) shows an increase of 16 and 22 dB in residual GL level for a micro-beamformer of three and four elements, respectively.

The channel count is reduced from 1152 (the number of elements) by a factor corresponding to the micro-beamformer size. Since a 10-Fr intracardiac catheter with a diameter of 3.3 mm limits the number of data transferring channels to around 100 micro-coaxial cables [34], the total reduction factor should be at least 12 to account for additional control signals and power supplies. A further on-chip reduction by at least a factor of 4 is thus required to reduce the channel count sufficiently. This can be achieved by methods such as analog time-division multiplexing [40], in-probe digitization combined with digital multiplexing [30], [32], or coding of the digitized signal [41].

In conclusion, the results show a feasible solution for intracardiac 3-D EWI. The 1-D micro-beamforming approach, in combination with on-chip channel-count reduction, can sufficiently reduce the data rate for transfer over a 10-Fr intracardiac catheter, while the proposed fan-shaped transmit beams and weighted averaging function preserve the image quality. The proposed method has the potential to offer single-beat 3-D EWI of the left atrium.

## Appendix A
## Fan-Shaped Transmit Beam Generation

To calculate a set of delays required for generating the desired beam, first, a virtual source location was determined based on beam divergence, transducer size, and steering direction in elevation; then, the transducer effective size in azimuth was determined based on the virtual source location and azimuthal beam divergence (see Fig. 13). The virtual source location was calculated by

$$\begin{cases} X_{\mathrm{vs}} = -sign(\theta)\dfrac{L_{\mathrm{e}\,1}\tan|\theta|}{\tan|\theta| - \tan(|\theta| - \varphi_{\mathrm{e}\,1})}; & Z_{\mathrm{vs}} = \dfrac{X_{\mathrm{vs}}}{\tan\varphi_{\mathrm{e}\,1}} \quad \theta \neq 0 \\ X_{\mathrm{vs}} = 0; & Z_{\mathrm{vs}} = \dfrac{L_{\mathrm{e}\,1}}{\tan\varphi_{\mathrm{e}\,1}} \quad \theta = 0 \end{cases} \tag{3}$$

where $\theta$ is the steering angle with a counterclockwise direction from the axial direction, $\varphi_{\mathrm{el}}$ is the beam divergence in elevation from a center line to a $-6$-dB contour, and $L_{\mathrm{el}}$ is half of the transducer size in elevation. The $Y$-coordinate value of the virtual source was always 0 because there was no transmit beam steering in the azimuth dimension. Having the virtual source location, the effective transducer size in azimuth was calculated by

$$L_{\mathrm{az}} = R_{\mathrm{vs}}\tan(\varphi_{\mathrm{az}}); \quad R_{\mathrm{vs}} = \sqrt{X_{\mathrm{vs}}^2 + Z_{\mathrm{vs}}^2} \tag{4}$$

where $L_{\mathrm{az}}$ is half of the effective aperture size in azimuth and $\varphi_{\mathrm{az}}$ is the beam divergence in azimuth from a center line to a 6-dB contour.

## References


[1] J. Jalife, "Mother rotors and fibrillatory conduction: A mechanism of atrial fibrillation," *Cardiovascular Res.*, vol. 54, no. 2, pp. 204–216, May 2002.

[2] M. Haïssaguerre *et al.*, "Mapping-guided ablation of pulmonary veins to cure atrial fibrillation," *Amer. J. Cardiol.*, vol. 86, no. 9, pp. K9–K19, Nov. 2000.

[3] A. Yaksh *et al.*, "A novel intra-operative, high-resolution atrial mapping approach," *J. Interventional Cardiac Electrophysiol.*, vol. 44, no. 3, pp. 221–225, Dec. 2015.

[4] M. Allessie and N. de Groot, "CrossTalk opposing view: Rotors have not been demonstrated to be the drivers of atrial fibrillation," *J. Physiol.*, vol. 592, no. 15, pp. 3167–3170, Aug. 2014.

[5] J. Sra and M. Akhtar, "Mapping techniques for atrial fibrillation ablation," *Current Problems Cardiol.*, vol. 32, no. 12, pp. 669–767, Dec. 2007.

[6] H. Ashikaga, B. A. Coppola, B. Hopenfeld, E. S. Leifer, E. R. McVeigh, and J. H. Omens, "Transmural dispersion of myofiber mechanics: Implications for electrical heterogeneity *in vivo*," *J. Amer. College Cardiol.*, vol. 49, no. 8, pp. 909–916, 2007.

[7] E. E. Konofagou and J. Provost, "Electromechanical wave imaging for noninvasive mapping of the 3D electrical activation sequence in canines and humans *in vivo*," *J. Biomech.*, vol. 45, no. 5, pp. 856–864, Mar. 2012.

[8] E. McVeigh, O. Faris, D. Ennis, P. Helm, and F. Evans, "Electromechanical mapping with MRI tagging and epicardial sock electrodes," *J. Electrocardiol.*, vol. 35, p. 61, Oct. 2002.

[9] O. P. Faris *et al.*, "Novel technique for cardiac electromechanical mapping with magnetic resonance imaging tagging and an epicardial electrode sock," *Ann. Biomed. Eng.*, vol. 31, no. 4, pp. 430–440, Apr. 2003.

[10] B. T. Wyman, W. C. Hunter, F. W. Prinzen, and E. R. McVeigh, "Mapping propagation of mechanical activation in the paced heart with MRI tagging," *Amer. J. Physiol.-Heart Circulatory Physiol.*, vol. 276, no. 3, pp. H881–H891, Mar. 1999.

[11] F. R. Badke, P. Boinay, and J. W. Covell, "Effects of ventricular pacing on regional left ventricular performance in the dog," *Amer. J. Physiol.-Heart Circulatory Physiol.*, vol. 238, no. 6, pp. H858–H867, Jun. 1980.

[12] M. Pernot and E. E. Konofagou, "Electromechanical imaging of the myocardium at normal and pathological states," in *Proc. IEEE Ultrason. Symp.*, Sep. 2005, pp. 1091–1094.

[13] L. Melki *et al.*, "Localization of accessory pathways in pediatric patients with Wolff-Parkinson-White syndrome using 3D-rendered electromechanical wave imaging," *JACC, Clin. Electrophysiol.*, vol. 5, no. 4, pp. 427–437, Apr. 2019.

[14] P. Nauleau, L. Melki, E. Wan, and E. Konofagou, "Technical note: A 3-D rendering algorithm for electromechanical wave imaging of a beating heart," *Med. Phys.*, vol. 44, no. 9, pp. 4766–4772, Sep. 2017.

[15] J. Provost *et al.*, "Assessing the atrial electromechanical coupling during atrial focal tachycardia, flutter, and fibrillation using electromechanical wave imaging in humans," *Comput. Biol. Med.*, vol. 65, pp. 161–167, Oct. 2015.

[16] J. Provost, V. Gurev, N. Trayanova, and E. E. Konofagou, "Mapping of cardiac electrical activation with electromechanical wave imaging: An in silico–*in vivo* reciprocity study," *Heart Rhythm*, vol. 8, no. 5, pp. 752–759, May 2011.

[17] J. Provost, W.-N. Lee, K. Fujikura, and E. E. Konofagou, "Imaging the electromechanical activity of the heart *in vivo*," *Proc. Nat. Acad. Sci. USA*, vol. 108, no. 21, pp. 8565–8570, May 2011.

[18] J. Provost *et al.*, "Electromechanical wave imaging for arrhythmias," *Phys. Med. Biol.*, vol. 56, no. 22, pp. L1–L11, Nov. 2011.

[19] J. Provost, S. Thiébaut, J. Luo, and E. E. Konofagou, "Single-heartbeat electromechanical wave imaging with optimal strain estimation using temporally unequispaced acquisition sequences," *Phys. Med. Biol.*, vol. 57, no. 4, p. 1095, 2012.

[20] A. Costet, E. Wan, E. Bunting, J. Grondin, H. Garan, and E. Konofagou, "Electromechanical wave imaging (EWI) validation in all four cardiac chambers with 3D electroanatomic mapping in canines *in vivo*," *Phys. Med. Biol.*, vol. 61, p. 8105, Oct. 2016.

[21] J. Grondin, D. Wang, C. S. Grubb, N. Trayanova, and E. E. Konofagou, "4D cardiac electromechanical activation imaging," *Comput. Biol. Med.*, vol. 113, Oct. 2019, Art. no. 103382.

[22] D. Wildes *et al.*, "4-D ICE: A 2-D Array transducer with integrated ASIC in a 10-Fr catheter for real-time 3-D intracardiac echocardiography," *IEEE Trans. Ultrason., Ferroelectr., Freq. Control*, vol. 63, no. 12, pp. 2159–2173, Dec. 2016.

[23] R. Fontes-Carvalho, F. Sampaio, J. Ribeiro, and V. G. Ribeiro, "Three-dimensional intracardiac echocardiography: A new promising imaging modality to potentially guide cardiovascular interventions," *Eur. Heart J. Cardiovasc. Imag.*, vol. 14, p. 1028, Oct. 2013.

[24] M. Alkhouli, T. Simard, A. M. Killu, P. A. Friedman, and R. Padang, "First-in-Human use of a novel live 3D intracardiac echo probe to guide left atrial appendage closure," *JACC, Cardiovascular Intervent.*, vol. 14, no. 21, pp. 2407–2409, Nov. 2021.

[25] G. Montaldo, M. Tanter, J. Bercoff, N. Benech, and M. Fink, "Coherent plane-wave compounding for very high frame rate ultrasonography and transient elastography," *IEEE Trans. Ultrason., Ferroelectr., Freq. Control*, vol. 56, no. 3, pp. 489–506, Mar. 2009.

[26] P. Santos, G. U. Haugen, L. Lovstakken, E. Samset, and J. D'hooge, "Diverging wave volumetric imaging using subaperture beamforming," *IEEE Trans. Ultrason., Ferroelectr., Freq. Control*, vol. 63, no. 12, pp. 2114–2124, Dec. 2016.

[27] C. Chen *et al.*, "A pitch-matched front-end ASIC with integrated subarray beamforming ADC for miniature 3-D ultrasound probes," *IEEE J. Solid-State Circuits*, vol. 53, no. 11, pp. 3050–3064, Nov. 2018.

[28] S. A. Scampini, "Microbeamforming transducer architecture," U.S. Patents 20080262351 A1, Oct. 23, 2008.

[29] J. D. Larson III, "2-D phased array ultrasound imaging system with distributed phasing," U.S. Patents 5229933, Jul. 20, 1993.

[30] D. Bera *et al.*, "Fast volumetric imaging using a matrix transesophageal echocardiography probe with partitioned transmit–receive array," *Ultrasound Med. Biol.*, vol. 44, no. 9, pp. 2025–2042, Sep. 2018.

[31] Y. Chen, L. Tong, A. Ortega, J. Luo, and J. D'hooge, "Feasibility of multiplane-transmit beamforming for real-time volumetric cardiac imaging: A simulation study," *IEEE Trans. Ultrason., Ferroelectr., Freq. Control*, vol. 64, no. 4, pp. 648–659, Apr. 2017.

[32] G. Gurun *et al.*, "Single-chip CMUT-on-CMOS front-end system for real-time volumetric IVUS and ICE imaging," *IEEE Trans. Ultrason., Ferroelectr., Freq. Control*, vol. 61, no. 2, pp. 239–250, Feb. 2014.

[33] Y. Hopf *et al.*, "A pitch-matched ASIC with integrated 65 V TX and shared hybrid beamforming ADC for catheter-based high-frame-rate 3D ultrasound probes," in *IEEE Int. Solid-State Circuits Conf. (ISSCC) Dig. Tech. Papers*, Feb. 2022, pp. 494–496.

[34] W. Lee, S. F. Idriss, P. D. Wolf, and S. W. Smith, "A miniaturized catheter 2-D array for real-time, 3-D intracardiac echocardiography," *IEEE Trans. Ultrason., Ferroelectr., Freq. Control*, vol. 51, no. 10, pp. 1334–1346, Oct. 2004.

[35] J. A. Jensen, "Field: A program for simulating ultrasound systems," in *Proc. 10th NordicBaltic Conf. Biomed. Imag.*, 1996, pp. 351–353.

[36] M. van Wijk and J. M. Thijssen, "Performance testing of medical ultrasound equipment: fundamental vs. harmonic mode," *Ultrasonics*, vol. 40, no. 1, pp. 585–591, 2002.

[37] T. Hergum, T. Bjastad, K. Kristoffersen, and H. Torp, "Parallel beamforming using synthetic transmit beams," *IEEE Trans. Ultrason., Ferroelectr., Freq. Control*, vol. 54, no. 2, pp. 271–280, Feb. 2007.

[38] Y. Zhang, Y. Guo, and W.-N. Lee, "Ultrafast ultrasound imaging using combined transmissions with cross-coherence-based reconstruction," *IEEE Trans. Med. Imag.*, vol. 37, no. 2, pp. 337–348, Feb. 2018.

[39] A. Rodriguez-Molares, J. Avdal, H. Torp, and L. Lovstakken, "Axial lobes in coherent plane-wave compounding," in *Proc. IEEE Int. Ultrason. Symp. (IUS)*, Sep. 2016, pp. 1–4.

[40] Q. Liu, C. Chen, Z.-Y. Chang, C. Prins, and M. A. P. Pertijs, "A mixed-signal multiplexing system for cable-count reduction in ultrasound probes," in *Proc. IEEE Int. Ultrason. Symp. (IUS)*, Oct. 2015, pp. 1–4.

[41] Z. Chen *et al.*, "Impact of bit errors in digitized RF data on ultrasound image quality," *IEEE Trans. Ultrason., Ferroelectr., Freq. Control*, vol. 67, no. 1, pp. 13–24, Jan. 2020.

**Mehdi Soozande** (Student Member, IEEE) received the B.Sc. degree in electrical engineering from the University of Sistan and Baluchestan, Zahedan, Iran, in 2011, and the M.Sc. degree in biomedical engineering from the Tehran University of Medical Sciences, Tehran, Iran, in 2015.

He worked as a Researcher with the Thoraxcenter Biomedical Engineering Department, Erasmus MC, Rotterdam, The Netherlands, from 2017 to 2021. In 2021, he joined Nearfield Instruments, Rotterdam, as an Ultrasound/Acoustic Researcher. His current research interests include GHz ultrasound imaging for NDT in semiconductor industry, advanced beamforming techniques, and atomic force microscopy.

**Boudewine W. Ossenkoppele** (Graduate Student Member, IEEE) received the B.Sc. degree in aerospace engineering and the M.Sc. degree in mechanical engineering from the Delft University of Technology, Delft, The Netherlands, in 2015 and 2018, respectively, where she is currently pursuing the Ph.D. degree with the Laboratory of Medical Imaging, Department of Imaging Physics.

Her current research interests include high-frame-rate 3-D ultrasound imaging, beamforming algorithms, ultrasound transducer design, and deep learning for ultrasound signal processing.

**Yannick Hopf** (Graduate Student Member, IEEE) received the B.Sc. and M.Sc. degrees (*cum laude*) in electrical engineering from the Technical University of Darmstadt, Darmstadt, Germany, in 2014 and 2017, respectively. He is currently pursuing the Ph.D. degree in electrical engineering from the Electronic Instrumentation Laboratory, Delft University of Technology, Delft, The Netherlands, with a focus on application-specific integrated circuit (ASIC) design for 3-D high-frame-rate medical ultrasound imaging.

His current research interests include analog- and mixed-signal integrated circuits for ultrasound imaging, high-voltage electronics, and low-power analog to digital converters.

Mr. Hopf was honored with the Eckelmann AG Price for Best Degree for his M.Sc. graduation.

**Michiel A. P. Pertijs** (Senior Member, IEEE) received the M.Sc. and Ph.D. degrees (*cum laude*) in electrical engineering from the Delft University of Technology, Delft, The Netherlands, in 2000 and 2005, respectively.

In 2009, he joined the Electronic Instrumentation Laboratory, Delft University of Technology, where he is currently an Associate Professor. He also heads a research group focusing on integrated circuits for medical ultrasound and energy-efficient smart sensors.

Dr. Pertijs is a member of the Technical Program Committee of the European Solid-State Circuits Conference (ESSCIRC). He served on the program committees of the International Solid-State Circuits Conference (ISSCC) and the IEEE Sensors Conference. He received the ISSCC 2005 Jack Kilby Award and the IEEE JOURNAL OF SOLID-STATE CIRCUITS (JSSC) 2005 Best Paper Award. He served as an Associate Editor for the IEEE OPEN JOURNAL OF THE SOLID-STATE CIRCUITS SOCIETY (O-JSSC) and JSSC.

**Martin D. Verweij** (Member, IEEE) received the M.Sc. (*cum laude*) and Ph.D. degrees in electrical engineering from the Delft University of Technology, Delft, The Netherlands, in 1988 and 1992, respectively.

In 1998, he became an Associate Professor with the Laboratory of Electromagnetic Research, Delft University of Technology, where he joined the Laboratory of Acoustical Wavefield Imaging in 2011. Since 2021, he has been heading the Ultrasound Group, Department of Imaging Physics, Delft University of Technology. His current research interests include dedicated transducer designs, beamforming algorithms, and the theoretical modeling and numerical simulation of medical ultrasounds.

Dr. Verweij is a fellow and an Associate Editor of the *Journal of the Acoustical Society of America*.

**Nico de Jong** (Member, IEEE) received the M.Sc. degree in physics from the Delft University of Technology, Delft, The Netherlands, in 1978, and the Ph.D. degree in acoustic properties of ultrasound contrast agents from the Erasmus Medical Center (Erasmus MC), Rotterdam, The Netherlands, in 1993.

Since 1980, he has been a Staff Member with the Thoraxcenter, Erasmus MC. Since 2011, he has been a Professor in molecular ultrasonic imaging and therapy with Erasmus MC and the Delft University of Technology. From 2015 to 2021, he was the Head of the Medical Imaging Group, Delft University of Technology.

**Hendrik J. Vos** (Member, IEEE) received the M.Sc. degree in applied physics from the Delft University of Technology, Delft, The Netherlands, in 2004, and the Ph.D. degree from the Department of Biomedical Engineering, Erasmus Medical Center (MC), Rotterdam, The Netherlands, in 2010.

He worked as a Postmaster Researcher with the University of Florence, Florence, Italy; and a Contract Researcher for the petrochemical industry on cutting-edge ultrasonic solutions. He is currently an Associate Professor with Erasmus MC and the Delft University of Technology. His research interests include acoustical array technology for biomedical imaging in all its aspects: transducers, 2-D and 3-D beamforming, cardiac shear waves, ultrafast Doppler, contrast imaging, and related preclinical and clinical studies.

Dr. Vos received the Dutch NWOTTW VIDI Personal Grant in 2018.

**Johan G. Bosch** (Member, IEEE) received the M.Sc. degree in electrical engineering from the Eindhoven University of Technology, Eindhoven, The Netherlands, 1985, and the Ph.D. degree from Leiden University, Leiden, The Netherlands, 2006.

He is currently an Associate Professor with the Department of Biomedical Engineering, Thoraxcenter, Erasmus Medical Center (MC), Rotterdam, The Netherlands. He is also a (co-)PI of projects on 3-D ultrasound image formation, transducer development, 2-D and 3-D cardiovascular imaging, and flow and tissue stiffness assessment using novel ultrasound approaches. His research interests include echocardiographic image processing, transducer development, and novel ultrasound techniques for image formation and functional imaging.